

Optical Activity in Third-Harmonic Rayleigh Scattering: A New Route for Measuring Chirality

Lukas Ohnoutek, Hyeon-Ho Jeong, Robin Raffè Jones, Johannes Sachs, Ben J. Olohan, Dora-Maria Rășădean, Gheorghe Dan Pantoș, David L. Andrews, Peer Fischer, and Ventsislav K. Valev*

In 3D isotropic liquids, optical third-harmonic generation is forbidden, with circularly polarized light (CPL). Yet the associated nonlinear susceptibility directly influences the optical properties at the fundamental frequency by intensity dependence (Kerr effect). Here, the hidden third-harmonic optical properties upon CPL illumination are revealed by demonstrating a new effect, in hyper-Rayleigh scattering. This effect is succinctly enunciated: the intensity of light scattered at the third-harmonic frequency of the CPL incident light depends on the chirality of the scatterers. It is referred to as third-harmonic (hyper) Rayleigh scattering optical activity (THRS OA) and was observed from Ag nanohelices randomly dispersed in water. The first analytical theory model for the new effect in nanohelices is also provided, highlighting the role of localized transition dipoles along the helical length. THRS OA is remarkably user-friendly. It offers access to intricate optical properties (hyperpolarizabilities) that have so far been more easily accessible by computation and that are essential for the understanding of light–matter interactions. The new effect could find applications in hyper-sensitive characterization of the chirality in molecules and in nanostructures; this chirality plays a fundamental role in the function of bio/nano-machinery, with promising applications in next generation technologies.

1. Introduction

Chirality – the lack of mirror symmetry – is exhibited at all scales in nature. It is present in sub-atomic particles,^[1] in amino acids and DNA,^[2] in snail shells,^[3] in local tornadoes and planetary cyclones,^[4] and in solar systems and spiral galaxies as they travel through space. Coming full circle, the galaxy chirality might have originated from chiral sub-atomic interactions in the early Universe.^[5] Like the shape of human hands, many biological objects are chiral and each chiral form is said to exhibit “handedness;” for instance, all sugars, including ribose that forms the backbone of DNA, are defined as right-handed based on their interaction with polarized light. The chirality of molecules can be of vital importance, as illustrated by pharmaceuticals such as Thalidomide,^[6] Naproxen,^[7] Levodopa,^[8] and Penicillamine,^[9] whose mirror-images can cause birth defects,

L. Ohnoutek, R. R. Jones, B. J. Olohan, V. K. Valev
Centre for Photonics and Photonic Materials
University of Bath
Bath BA2 7AY, UK
E-mail: V.K.Valev@bath.ac.uk

L. Ohnoutek, R. R. Jones, B. J. Olohan, V. K. Valev
Centre for Nanoscience and Nanotechnology
University of Bath
Bath BA2 7AY, UK

H.-H. Jeong, J. Sachs, P. Fischer
Max Planck Institute for Intelligent Systems
Heisenbergstr. 3, Stuttgart 70569, Germany


H.-H. Jeong
School of Electrical Engineering and Computer Science
Gwangju Institute of Science and Technology
Gwangju 61005, Republic of Korea

D.-M. Rășădean, G. D. Pantoș
Department of Chemistry
University of Bath
Bath BA2 7AY, UK

D. L. Andrews
School of Chemistry
University of East Anglia
Norwich Research Park, Norwich NR4 7TJ, UK

P. Fischer
Institute for Physical Chemistry
University of Stuttgart
Pfaffenwaldring 55, Stuttgart 70569, Germany

V. K. Valev
Centre for Therapeutic Innovation
University of Bath
Bath BA2 7AY, UK

 The ORCID identification number(s) for the author(s) of this article can be found under <https://doi.org/10.1002/lpor.202100235>

© 2021 The Authors. Laser & Photonics Reviews published by Wiley-VCH GmbH. This is an open access article under the terms of the Creative Commons Attribution License, which permits use, distribution and reproduction in any medium, provided the original work is properly cited.

DOI: 10.1002/lpor.202100235

liver poisoning, chronic bacterial infection, and neurotoxicity, respectively. Light can serve to identify the chirality of molecules.

Circularly polarized light (CPL) is also chiral.^[10] Noting that there are two directly opposite conventions in current usage, here we define left-handed CPL as follows: Looking from the point of view of the source, along the direction of propagation, the electric field of left-handed CPL traces a helix in space that curls anticlockwise. However, because of the large difference in scale between the chirality of molecules (a few nm) and light (hundreds of nm), the chiroptical interactions are usually very weak. Recent progress in nanotechnology has bridged this difference of scales.^[11,12]

Chiral nanostructures have at least one dimension in the range of 0.1–100 nm. Metal nanostructures usually have at least one dimension in the tens of nm. This confinement causes the electrons at the metal surface to oscillate coherently upon illumination with visible light, forming a surface plasmon resonance. Surface plasmons effectively compress the wavelength of light, thereby enabling novel and enhanced light-matter interactions. Chiral nanotechnology is currently driving interest in materials with negative refractive index,^[13] nanorobotics,^[14–16] chiral molecular sensing,^[17] and optical components for manipulating CPL, that can in turn find applications in spintronics^[18] and quantum-optical computing.^[19] It could enable hyper-sensitive characterization of molecular chirality (e.g., amino acids,^[20] proteins,^[21] and DNA)^[22] and of the chirality in nanostructures (including nanorobotic components^[14,22] and DNA origami assemblies);^[23] this chirality plays a key role in the function of bio/nano-machinery,^[24] with emerging applications in next generation technologies.^[11]

Another way to bridge wavelength scales resides in the nonlinear optical processes of harmonic generation and scattering, where n photons at the fundamental wavelength are annihilated to produce a single photon at the wavelength λ/n . Not surprisingly, the combination of these nonlinear optical effects with nanostructured materials and surface plasmon resonances leads to enhanced chiroptical interactions.^[25,26] However, whereas chiral (bio)molecules are naturally freely revolving in water, the artificially made chiral nanomaterials (or chiral “metamaterials”) consist of immobile nanoparticles, often arranged in well-ordered arrays, or rigid networks. This immobility and artificial order can result in the appearance of “false chirality,”^[27] anisotropy effects,^[28,29] linear dichroism, circular dichroism in the angular distribution of photoelectrons,^[30–33] pseudo chirality,^[34] or extrinsic chirality.^[35,36]

Observing optical activity in the nonlinear optical processes directly, using frequency conversion within liquids has been quite elusive. The possibility was first suggested in 1979^[37] but it took 40 years for an experimental demonstration using Ag nanohelices,^[38] emitting at the second harmonic frequency (i.e., for $n = 2$). Soon after, this second harmonic effect was observed in chiral molecules^[39] and in chiral gold cuboids.^[40]

Here, we report the first observation of chiroptical third-harmonic scattering (i.e., for $n = 3$), from a suspension of silver nanohelices in water. Because energy is conserved in both light and matter, this harmonic process is elastic and we refer to it as third-harmonic (hyper) Rayleigh scattering. Upon varying the fundamental wavelength, we demonstrate

that the measured signal is consistently emitted at $\lambda/3$. The intensity of the measured signal follows a cubic power law on the fundamental intensity. For a given handedness of the nanohelices, there is a clear difference in the measured signal depending on the chirality of light; upon reversing the handedness of the nanostructures, this difference reverses. No difference is observed upon illuminating a racemic mixture of chiral nanohelices, that is, a 50:50 mixture of both handednesses. We identify the origin of this new effect as an interplay between electric dipoles along the length of the nanohelices, as evidenced by theoretical calculations and rigorous numerical simulations.

The third-harmonic (hyper) Rayleigh scattering optical activity (THRS OA) effect reveals the most direct expression of the chiroptical nonlinearity. Until now, this chiroptical nonlinearity has only been known through phenomena, such as the intensity-dependent effect at the fundamental frequency,^[41–43] which affects both circular dichroism^[44] and optical rotation measurements.^[45] Such effects are indirect, as information on the nonlinearity needs to be separated from the linear behavior and the required high incident light intensity leads to thermal complications.^[46–48] By comparison, THRS OA measures directly chiroptical nonlinearity, at the third-harmonic, with zero background from the fundamental frequency. Third-harmonic generation (THG) circular dichroism^[26] is also a background-free chiroptical effect, however it requires emission coherence between its sources and it is forbidden in isotropic liquids—the medium of choice for chemistry and bio-technology. By contrast, THRS OA is an incoherent scattering effect in liquids. Other valuable nonlinear scattering chiroptical effects are two-photon absorption circular dichroism^[49–51] and circular differential two-photon luminescence;^[52] both are sensitive to the chiroptical nonlinearity, however they are non-elastic, that is, they require real energy states that restrict the frequencies at which these effects can be observed. At variance, THRS OA results from an elastic process, where the initial and final quantum mechanical states of the excited electrons are identical. Consequently, there is no restriction on the frequency of the incoming light, since only virtual states are involved.

2. Results

THRS OA is schematically illustrated in **Figure 1a**. CPL with wavelength λ is incident on a silver nanohelix, which leads to scattering at the third-harmonic wavelength $\lambda/3$. The intensity of the scattered light is dependent on the direction of circular polarization of the incident light. The measured difference in intensity of the scattered light thus provides information about the handedness of the scatterers.

The samples we investigate in this work are silver nanohelices suspended in an isotropic liquid. Their dimensions, indicated in **Figure 1b**, are much smaller than the wavelength of the incident light (i.e., $\lesssim \lambda/10$) and the nanoparticles can thus be regarded as meta-molecules. Scanning electron microscopy images of the nanohelices on a silicon wafer (**Figure 1c**) show well-defined geometry and good homogeneity over the imaged region for both of the chiral versions (enantiomorphs) of the nanohelices. The results of dynamic light scattering experiments (see **Figure 1d**)

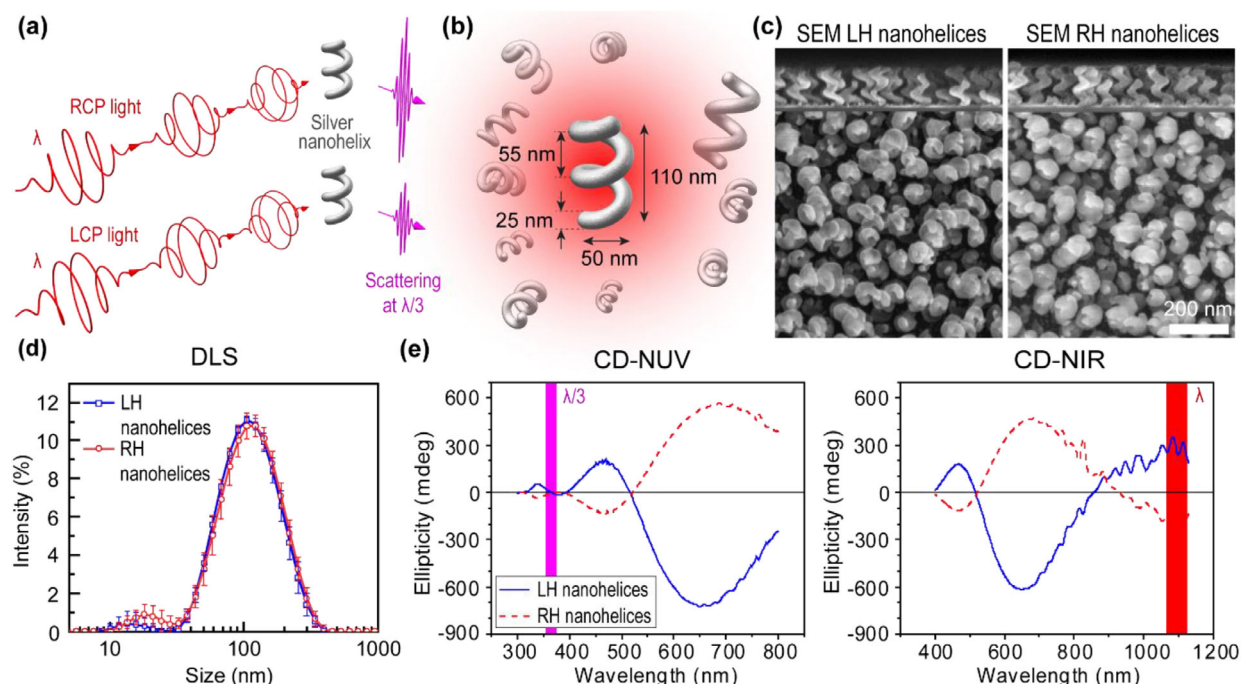


Figure 1. Well-defined silver nanohelices, which are investigated in our third-harmonic Rayleigh scattering optical activity (THRS OA) experiments. a) Schematic illustration of THRS OA. A silver nanohelix is illuminated with a laser beam with wavelength λ , which leads to scattering at the third-harmonic frequency (i.e., $\lambda/3$). The intensity of the scattered light depends on the polarization of the incident light (RCP = right circular polarization, LCP = left circular polarization). b) Dimensions of the silver nanohelices. c) Scanning electron microscopy (SEM) images of the nanohelices on a wafer. The top part of the image is a side-view, the lower part is an aerial view. LH = left-handed, RH = right-handed. d) Dynamic light scattering (DLS) in suspensions of the nanohelices. e) Linear optical regime ellipticity spectra of left- and right-handed nanohelices suspended in 1 mM trisodium citrate measured with a commercial circular dichroism (CD) spectrometer, in the near-ultraviolet (NUV) spectral region (left) and in the near-infrared (NIR) region (right). The red-shaded region corresponds to the wavelength range of the incident light in our THRS experiments. The violet-shaded region indicates the wavelength range of the detected light in these experiments.

performed on nanohelices in a suspension confirm the relatively narrow distribution in the sizes of the fabricated nanohelices. A close agreement between the results obtained for the left-handed and the right-handed nanohelices can also be seen.

The nanohelices have strong chiroptical properties in the linear regime, as demonstrated by Figure 1e. The graphs show the ellipticity (a measure of circular dichroism, see Section 5 for details) spectra from left- and right-handed nanohelices, plotted with continuous blue and dashed red lines, respectively. These measurements are obtained with a commercial CD spectrometer (see Section 5 for details). In order to cover the whole spectral range that is of interest for our third-harmonic experiments, two detectors are used, from 300 to 800 nm and from 400 to 1130 nm. The ellipticity spectra are clearly bisignate (in agreement with Kuhn's sum rule)^[53] and the spectra of the two enantiomorphs of the nanohelices present opposite signs, as expected.

The experimental apparatus for measuring THRS is illustrated in Figure 2. In essence, a circularly polarized laser beam is focused into a cuvette containing a suspension of Ag nanohelices. Scattered light is collected by a lens placed next to the side of the cuvette. Bandpass filters are placed in front of the light detector to select light in the desired wavelength range for detection. The setup is very user-friendly and could be widely adopted as a chiroptical measuring tool of molecular and nano-materials. A detailed description of the apparatus can be found in Section 5.

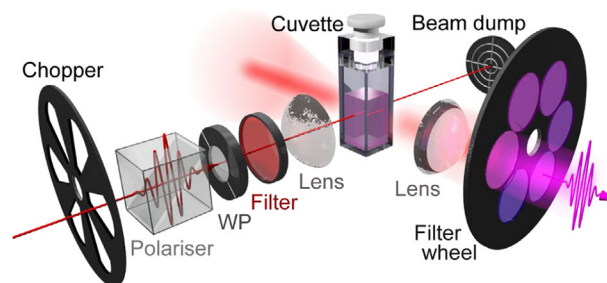


Figure 2. Illustration of the user-friendly experimental setup for measuring third-harmonic Rayleigh scattering. A laser beam, modulated by a chopper blade, passes through a polarizer and a quarter-wave plate (WP) to obtain circularly polarized light. A long-pass filter removes wavelengths below ≈ 950 nm from the laser beam. The beam is focused into a cuvette filled with a suspension of silver nanohelices and scattered light is collected perpendicularly to the incident beam. Bandpass filters are used to select light in a desired range of wavelengths for detection.

THRS ellipticity θ_{THRS} is calculated using the following formula:

$$\theta_{\text{THRS}} = \frac{180}{\pi} \arctan \left(\frac{\sqrt{I_{\text{RCP}}^{(3\omega)}} - \sqrt{I_{\text{LCP}}^{(3\omega)}}}{\sqrt{I_{\text{RCP}}^{(3\omega)}} + \sqrt{I_{\text{LCP}}^{(3\omega)}}} \right) \quad (1)$$

where $I_{\text{RCP}}^{(3\omega)}$ and $I_{\text{LCP}}^{(3\omega)}$ are the detected third-harmonic Rayleigh scattering intensities under illumination with right circularly polarized (RCP) and left circularly polarized (LCP) light, respectively.

As a third-order nonlinear optical process, THRS scales cubically with incident power. To verify this dependence and to rule out any significant laser-induced damage to the nanohelices, we measure THRS intensity as a function of incident laser power (up to 35 mW). In Figure 3a–c, the illumination wavelength is set to 1095 nm and the measured wavelength is 365 nm. The experiments are performed for left-handed nanohelices in (a), right-handed nanohelices in (b), and a racemic (i.e., 50:50) mixture of the two enantiomorphs in (c). All the data points are fitted with a cubic function and the corresponding R^2 values are shown in the figure insets, demonstrating a good agreement with a cubic power dependence. No significant laser damage can be observed (such damage usually results in a deviation from the expected power dependence, above the damage threshold).

Furthermore, in Figure 3a the detected intensity clearly depends on the direction of circular polarization of the incident light. This dependence is an indication of chiroptical interaction, however, it could also be due to the presence of unaccounted chirality in our setup. Importantly, in Figure 3b it is apparent that the difference reverses with the chirality of the samples. Also significant is the fact that, in the case of the racemic mixture in Figure 3c, the power dependence is cubic but there is no appreciable signal difference, depending on the direction of incident circular polarization. Therefore, there is no unaccounted chirality in our setup and the observed chiroptical signatures in Figure 3a,b can be attributed to the THRS OA effect. In each case, the corresponding THRS ellipticities (calculated using Equation (1)) are shown in the lower part of the figures. These ellipticities remain relatively constant, as a function of laser power. They are of $\approx \pm 3^\circ$ for left- and right-handed nanohelices, respectively and $\approx 0^\circ$ for the racemic mixture. The contribution of the solvent in which the nanohelices are dispersed (1 mM trisodium citrate) to the results presented in Figure 3 is negligible, as even at the maximum incident power (35 mW) the THRS intensity detected for pure solvent is on the order of 0.3 counts s^{-1} .

In order to clearly attribute the measured signal to third-harmonic scattering, this signal needs to be distinguishable from the multiphoton luminescence background and it needs to follow the frequency of illumination. Figure 3d presents the emission spectra of the nanohelices, for three illumination wavelengths: 1065, 1095, and 1125 nm. The emission is determined with the use of four bandpass filters, whose bandwidth is indicated by the horizontal error bars. The error bars along the vertical direction correspond to standard deviation. The data demonstrate a significant multiphoton emission background that increases with emission wavelength. However, for all three illumination wavelengths, the harmonic signal (indicated with violet vertical lines) is always above that background. Moreover, the intensity of this harmonic signal depends on the direction of CPL and this dependence reverses with the chirality of the samples. Therefore, we confirm that we have observed the THRS OA effect. Next, we examine the polarization of the THRS.

First, an analyzing quarter-wave plate (AQWP) is positioned between the collection lens and the analyzing polarizer (ana-

lyzer), then the polarizer and analyzer are crossed, with polarizer along the vertical (S) direction and analyzer along the horizontal (P) direction. THRS intensity measured for various angles of the AQWP is shown in Figure 4a,b for left-handed and right-handed nanohelices, respectively. The results confirm the THRS OA effect—there is a very clear difference of THRS intensity depending on the direction of polarization and handedness of the nanohelices. Moreover, the THRS intensity does not depend on the AQWP angle; only random variations are visible. This result demonstrates that for incident LCP and RCP light, the THRS is unpolarized.

The polarization of the THRS can be further quantified using the depolarization ratios. For this purpose, the AQWP is removed and the analyzer is placed between the collection lens and the filter wheel in Figure 2. Table 1 shows the THRS intensity measured for the main orientations of the polarizer and analyzer; S and P correspond to vertical and horizontal directions, respectively.

Depolarization ratios are defined as $\frac{\langle I_{\text{THRS}}^{\text{S}} \rangle}{\langle I_{\text{THRS}}^{\text{P}} \rangle}$ for incident P-polarized light and $\frac{\langle I_{\text{THRS}}^{\text{P}} \rangle}{\langle I_{\text{THRS}}^{\text{S}} \rangle}$ for incident S-polarized light, where $\langle I_{\text{THRS}}^{\text{P}} \rangle$ and $\langle I_{\text{THRS}}^{\text{S}} \rangle$ indicate an average THRS intensity measured with the analyzer oriented along P or S, respectively. For the left-handed nanohelices, $\frac{\langle I_{\text{THRS}}^{\text{S}} \rangle}{\langle I_{\text{THRS}}^{\text{P}} \rangle} = 0.87$ and $\frac{\langle I_{\text{THRS}}^{\text{P}} \rangle}{\langle I_{\text{THRS}}^{\text{S}} \rangle} = 0.82$. For the right-handed nanohelices, $\frac{\langle I_{\text{THRS}}^{\text{S}} \rangle}{\langle I_{\text{THRS}}^{\text{P}} \rangle} = 0.90$ and $\frac{\langle I_{\text{THRS}}^{\text{P}} \rangle}{\langle I_{\text{THRS}}^{\text{S}} \rangle} = 0.97$. All depolarization ratios are close to 1, indicating that due to the orientational averaging effect, the particulate medium is close to centrosymmetric, which is a good effective approximation of Pendry's "chiral spheres."^[13]

Next, we address a possible alternative explanation: Our result could be produced by coherent, forward-propagating THG from the glass interfaces, followed by linear optical regime Rayleigh scattering.^[54] To rule out this possibility, we rebuild the detection arm of our experiment and examine the forward emission signal, at the third-harmonic wavelength.

Figure 4c presents the schematic diagram of a THG setup. Upon varying the position of the focusing lens, for linearly polarized light at 1095 nm, THG is observed from the 4 interfaces of the cuvette: air/SiO₂, SiO₂/water, water/SiO₂, and SiO₂/air. This THG signal is shown in Figure S1a, Supporting Information. However, upon illumination with LCP, the THG signal decreases by >2 orders of magnitude. Therefore, it is impossible for CPL from the interfaces to produce enough THG to account for the scattering we observe in Figure 3.

Figure 4d shows the forward emission at the third-harmonic wavelength. Specifically, the figure presents the third-harmonic intensity as a function of incident laser power, for LCP and RCP light at 1095 nm. Upon comparing with Figure 3a, it is immediately apparent that the forward emission signal is much smaller. All lines in Figure 4d are fits to the cubic function $y = Ax^3$. For both the left- and right-handed nanohelices, a minuscule amount of OA appears to be present and its sign matches that of the THRS OA, see Figure 3a,b. This forward emission signal could be attributed to a multiple particle scattering or to the lightning rod effect (e.g., from the tips of the nanohelices). Importantly, no strong THG signal is present and therefore we can conclude that the results in Figure 3 are due to the THRS OA effect. The

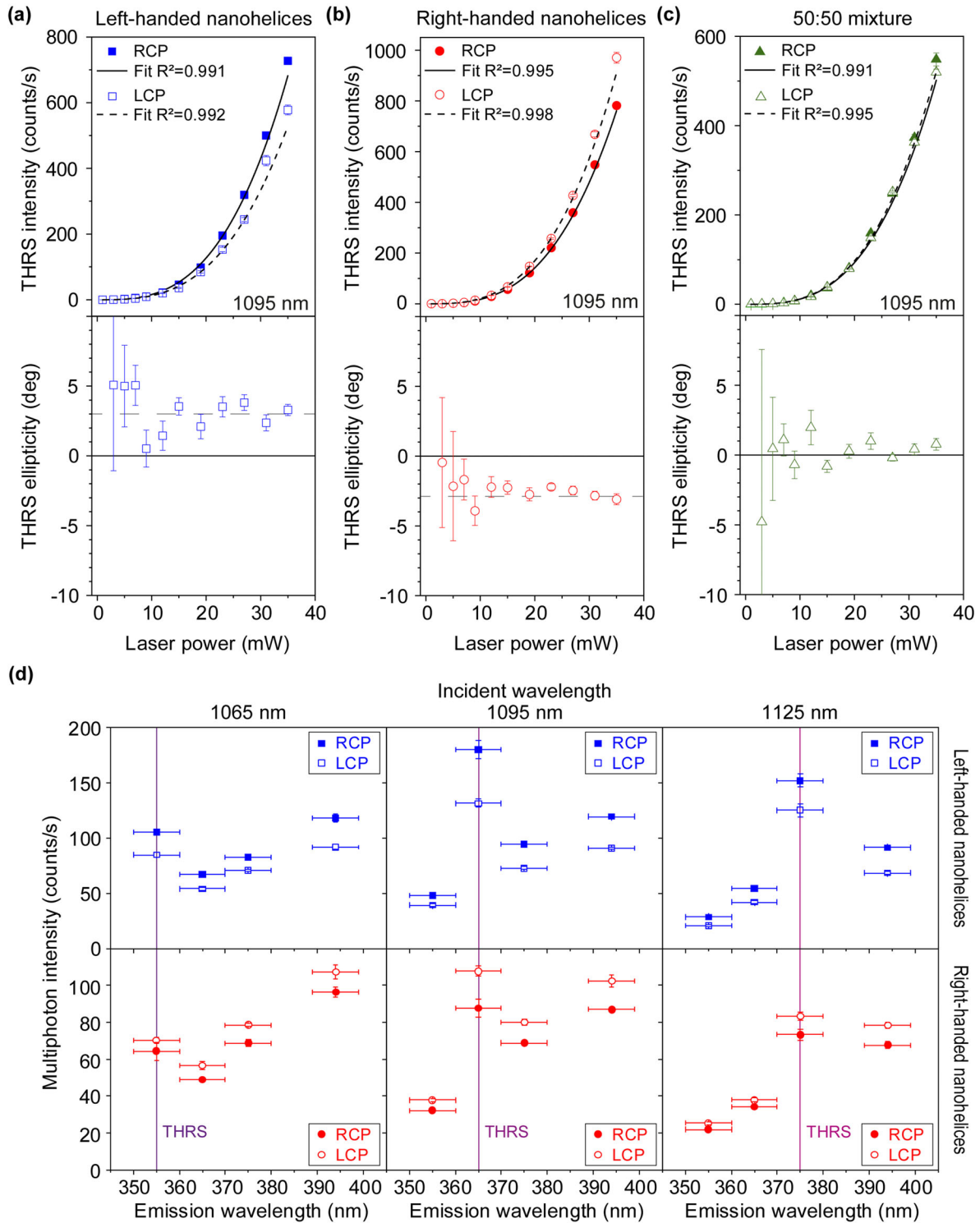


Figure 3. Clear third-harmonic Rayleigh scattering optical activity in suspensions of silver nanohelices. a–c) In the top panels, third-harmonic Rayleigh scattering (THRS) intensity plotted as function of incident power for the left- and right-handed nanohelices and for a 50:50 mixture of the enantiomorphs, respectively. THRS intensity is measured as a function of power for left circular polarization (LCP) and right circular polarization (RCP) of the incident light at a wavelength of 1095 nm. The error bars represent the standard deviation based on 6 measurements. The solid and dashed lines are best fits with the function $y = Ax^3$. Bottom panels: THRS ellipticity calculated for suspensions of the left-handed nanohelices, right-handed nanohelices, and a 50:50 mixture of the enantiomorphs, respectively. The dashed gray horizontal lines are guides for eye. d) Emission spectra of suspensions of left-handed (top panels) and right-handed nanohelices (bottom panels) when illuminated with light of a fixed wavelength (1065, 1095, or 1125 nm). The vertical error bars represent the standard deviation based on six measurements. The horizontal error bars indicate the bandwidth of the filters used for detection. The violet vertical lines indicate the third-harmonic wavelength of the incident light.

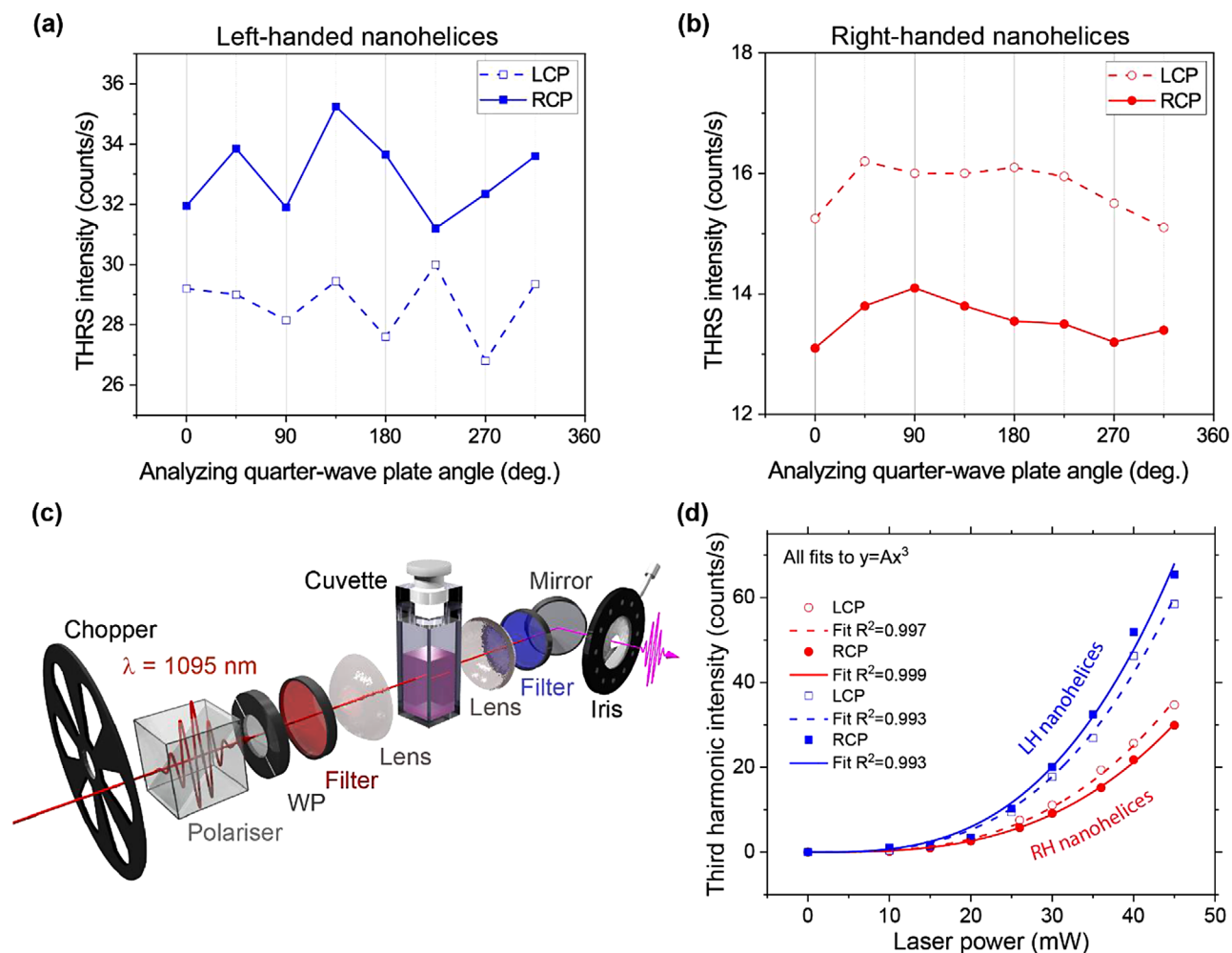


Figure 4. THRS polarization and forward emission. Measurements of third-harmonic Rayleigh scattering (THRS) intensity as a function of the angle of an analyzing quarter-wave plate (AQWP) for a) left-handed and b) right-handed nanohelices, upon illumination with left-circularly polarized (LCP) and right-circularly polarized (RCP) light at 1095 nm. The AQWP is positioned in the detection arm of the setup after the collection lens. At the angle of 0°, the fast axis of the AQWP is oriented along the horizontal (P) direction. The AQWP is followed by an analyzing polarizer, whose transmission axis is fixed along the horizontal (P) direction. c) A schematic diagram of the third-harmonic generation (THG) and forward emission setup. WP: quarter-wave plate. d) Third-harmonic intensity as a function of incident power for left-handed (LH) and right-handed (RH) nanohelices, upon illumination with LCP and RCP light. The lines are best fits to the function $y = Ax^3$. The illumination laser wavelength λ is 1095 nm.

Table 1. Detected THRS intensity from suspensions of left-handed and right-handed Ag nanohelices illuminated with P-polarized (P_{in}) or S-polarized (S_{in}) light at 1095 nm; an analyzing polarizer with its transmission axis oriented along the P- (P_{out}) or S- (S_{out}) direction is placed before the detector; the THRS intensity is in the units of counts s^{-1} .

	Left-handed nanohelices		Right-handed nanohelices	
	P_{out}	S_{out}	P_{out}	S_{out}
P_{in}	165.7	144.3	151.3	136.6
S_{in}	130.3	159.4	124.4	128.5

conclusion is supported by several control experiments that are detailed in Figure S2, Supporting Information. Next, we need to address the physical origin of THRS OA.

Drawing on fundamental electrodynamic and symmetry principles, theory has been developed to describe THRS from

molecules, focusing on its detailed dependence on both polarization and on properties of the nonlinear optical susceptibility tensor $\chi^{(3)}(-3\omega; \omega, \omega, \omega)$ for the scattering centres.^[55] More recently, this analysis has been extended specifically to elicit mechanisms and features uniquely associated with chiral species,^[56] here we extend the theory to the case of nanohelices.

For particles, such as small molecules compared to the wavelength of light, rigorously described in terms of multipole coupling,^[57] chiroptical effects primarily emerge from the interference of electric dipole (E1) and two other forms of coupling: magnetic dipole (M1) and electric quadrupole (E2).^[58] Since THRS is a four-photon process with a quantum amplitude dominated by $E1^4$ couplings, the relevant chiroptical interferences are $E1^4-E1^3M1$, and $E1^4-E1^3E2$. To exhibit the observed discrimination in handedness, the M1 or E2 interactions must couple with one of the incoming circularly polarized photons. For long-wavelength IR light, the E2 coupling is much less significant

than M1. It is therefore the $E1^3M1/E1^4$ terms that dominate the relative circular differential, g_{THRS} , which is defined as:

$$g_{\text{THRS}} = 2 \left(I_{\text{RCP}}^{(3\omega)} - I_{\text{LCP}}^{(3\omega)} \right) / \left(I_{\text{RCP}}^{(3\omega)} + I_{\text{LCP}}^{(3\omega)} \right) \quad (2)$$

whose values lie in the range $(-2,2)$.

These features underpin the computations of electric near-fields in the present work, where the electronic response of the metal to the circular electromagnetic fields of the input extends through the entirety of each nanohelix. We develop the long-established two-group model of optical activity,^[59] here adapted for electronically continuous media. Until the techniques were perfected for the nanofabrication of metal nanohelices,^[15] there were no media for which such a development was necessary; a basis for describing the circular dichroism of such systems has only recently been introduced.^[60]

For simplicity in the present account, we consider the electromagnetic influence of a beam propagating along the long helix axis, labelled z . The helix is initially described as a series of discrete transition dipoles,^[14,61,62] with the limiting case of a continuous medium to be taken in a subsequent integral form. Replacing a local M1 transition dipole interaction $\mathbf{m}^{(1)}$ with an equivalent, displaced E1 transition dipole $\boldsymbol{\mu}^{(2)}$ (dissymmetrically displaced from it at a distance R_{12}) we find for the particular case of response to CPL, $m_x^{(1)} \equiv ic\mu_y^{(2)}kR_{12}$; $m_y^{(1)} \equiv -ic\mu_x^{(2)}kR_{12}$, where x and y are coordinates in the transverse plane, and $k = 2\pi/\lambda$, where λ is the input wavelength. The linear dependence on distance in these expressions is valid only within the near-zone range $kR_{12} < 1$, where retardation effects can be ignored; this is a condition that holds for all distances between points on the nanohelices that are the subject of the present study.

A helix of pitch p and radius r , and with t the number of twists along its length, is assumed for present simplicity to be a wire-like helix of negligible cross-section, so that locally the discrete transition dipoles lie along the path of the coil. These assumptions lead to the following integral as a measure of the chiral response:

$$g_{\text{THRS}} \cong kp \int_0^{2\pi t} \sin \phi \cos \phi \left[\phi^2 + (4\pi r \sin(\phi/2)/p)^2 \right] d\phi \quad (3)$$

This limit indicates the maximum relative efficiency of converting one handedness of circular polarization compared to the other. The ellipticity values can be related to g_{THRS} using the relation:

$$\theta_{\text{THRS}} = \frac{180}{\pi} \arctan \left(\frac{\sqrt{g_{\text{THRS}} + 2} - \sqrt{2 - g_{\text{THRS}}}}{\sqrt{g_{\text{THRS}} + 2} + \sqrt{2 - g_{\text{THRS}}}} \right) \quad (4)$$

For the dimensions of the nanohelices in the present study, distributed about an average with $r = 25$ nm, $p = 55$ nm, and $t = 2$, the results indicate limits on the permissible extent of chiral discrimination of an ideal system—almost complete chiral selectivity. For 1065 nm input the calculated ellipticity is $+7.36^\circ$. The linear dependence of g_{THRS} on the input wavenumber leads to slightly lower ellipticity values for the higher input wavelengths. The physical effects of dispersion are not accounted for

at this level of theory. The experimental values indicate an ellipticity of $\approx 3^\circ$ (specifically, the median values are $\theta_{\text{THRS}}^{\text{LH}} = +3.5^\circ$, $\theta_{\text{THRS}}^{\text{RH}} = -2.25^\circ$, and $\theta_{\text{THRS}}^{\text{MIX}} = 0.4^\circ$). The highest of these values indicates a propensity for approaching the maximum degree of chiral response; the experimental attainment of such optimal values may require the fabrication of more slender nanohelices with smaller coil cross-sections. The presence of electric dipoles in our nanohelices is illustrated with numerical simulations of the near-fields.

Figure 5 presents numerical simulation results of the electric near-fields, around a left-handed silver nanohelix, viewed in the y - z plane. The electric fields viewed in the x - z and x - y planes are presented in Figures S3 and S4, Supporting Information, respectively. The color-coded intensities follow the rainbow order, with violet being the maximum. The three panels on the left correspond to illumination with LCP and those on the right correspond to illumination with RCP light. In the top two panels, the propagation vector (\mathbf{k}) is parallel to the Cartesian x -axis. In the middle two panels, \mathbf{k} is parallel to the Cartesian y -axis and, in the bottom two panels, \mathbf{k} is parallel to the Cartesian z -axis, which is the axis of the nanohelix.

For illumination at 1095 nm, Figure 5a shows clearly localized electric fields that are radiated by localized electric dipole oscillations discussed earlier. Additionally, for \mathbf{k} parallel to x and to z , strong electric field hotspots can be observed at the end termination of the helix, where a lightning rod effect can take place, as discussed above. Moreover, regardless of the direction of \mathbf{k} , the local electric fields are larger upon illumination with RCP, which suggests a preferential light-matter interaction and is in agreement with Figure 3d.

Results of simulations of the same nanohelix illuminated with 365-nm light are presented in Figure 5b. The data are organized similarly to those in Figure 5a. Again, clear local electric fields are evidenced, however the dependence on the direction of CPL is less clear, in agreement with the results in Figure 1e.

3. Discussion

Here, we unambiguously demonstrate the new chiroptical effect of THRS OA. For this purpose, it is crucial that the detected signal is as unaffected as possible, between its source and the detector. We have therefore carefully selected our fundamental and harmonic wavelengths, avoiding any strong linear regime chiroptical effects at the third-harmonic wavelength, see Figure 1e. Such effects can of course be accounted for, but for the present work they constitute an unnecessary complication.

Besides tuning the wavelength, several other parameters can be optimized in order to improve the sensitivity of the technique. For instance, as Figure 3 indicates, larger incident laser power will result in a dramatically increased detected signal. This is particularly promising since no optically induced damage has been observed so far. It would also be important to investigate the influence of the laser pulse duration, by comparing fs and ps illumination at the same average laser power.

The volume of illumination versus the concentration of nanohelices can also be optimized. In this work, the illumination volume in focus (V_{focus}) is estimated based on both a measurement and a calculation of the Rayleigh range (z_R), see Figure S5, Supporting Information, and the related discussion in the

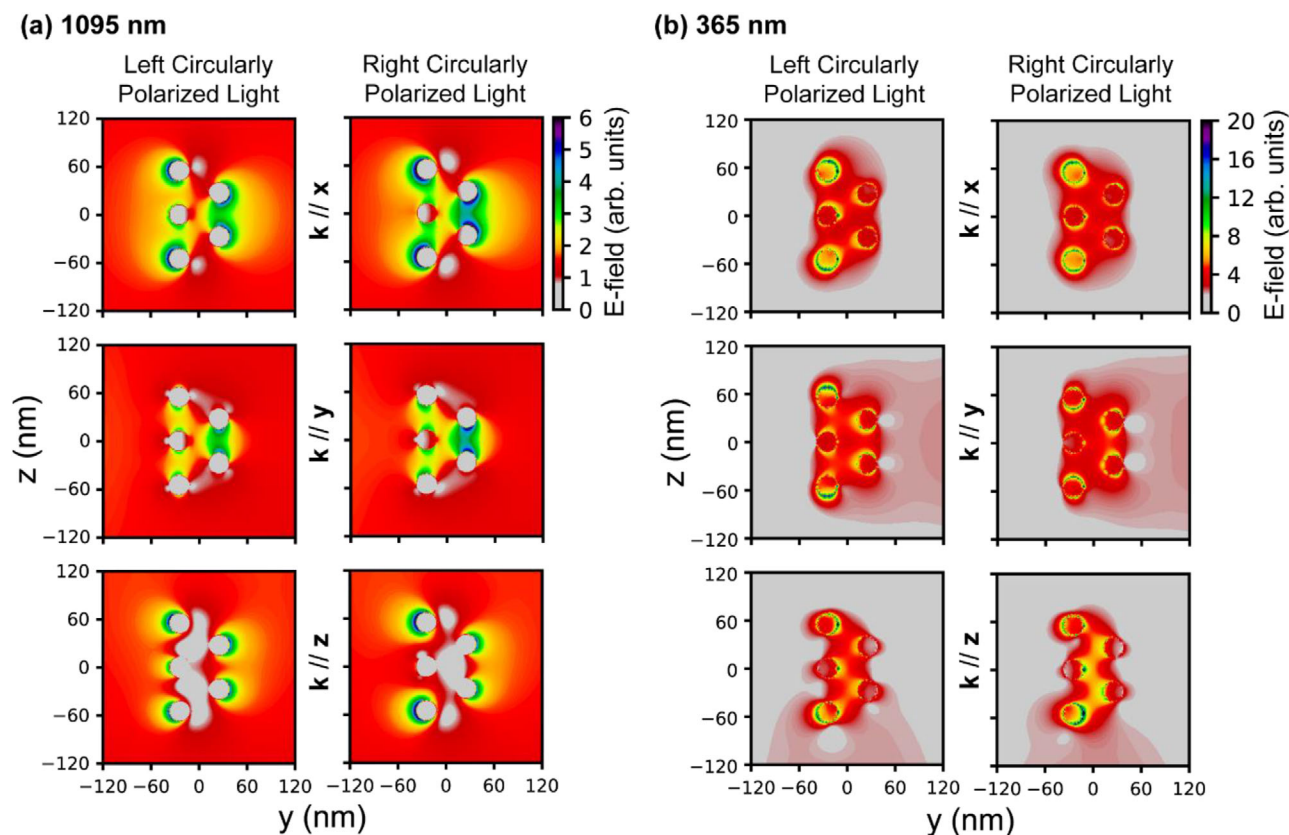


Figure 5. Strongly localized electric near-fields surround the silver nanohelices and depend on the direction of circularly polarized illumination. For incident wavelength at 1095 and 365 nm, in a) and b), respectively, the 6 panels in each of the figures present the amplitude of the electric near-field in the y - z plane for left circularly polarized (in the left panels) and right circularly polarized (in the right panels) light. Top, light propagating with k vector along (parallel to) the x axis; middle light propagating with k vector along the y axis; bottom, light propagating with k vector along the z axis, which is the long axis of the nanohelix.

Supporting Information. Upon integrating the beam area around the beam waist, from $-z_R$ to $+z_R$, we find $V_{\text{focus}} = 4.56 \times 10^{-14} \text{ m}^3$. The concentration of the nanohelices is estimated from the surface area of the sample wafers, using geometry considerations, see Supporting Information. For left- and right-handed nanohelices, we obtain concentrations of 1.15×10^{16} nanohelices m^{-3} and 8.35×10^{15} nanohelices m^{-3} , respectively. For all samples measured in this work, we estimate that the number of nanohelices in V_{focus} is between 400 and 700. In order to record larger values of the nonlinear optical ellipticity θ_{THRS} , the nanohelix geometry can also be tuned and the simplicity of our analytical model affords physical insights.

First, at this level of approximation it transpires that for all physically realistic dimensions the integral in Equation (3) is relatively insensitive to the pitch angle, which is given by $\tan^{-1}(p/2\pi r)$. In fact, as t increases, the integral converges to a value of approximately $\pi t/2$. Since $pt = L$, the length of the helix, this signifies that $g_{\text{THRS-CD}} = 1/2kL$ represents a near-zone limit that is essentially independent of the pitch angle. For example, a nanohelix composed of twice the length of coil, but wound more tightly to keep to the same external dimensions, can therefore be expected to display a similar level of chiral discrimination. This can readily be understood; although a greater length affords more pair-elements to exhibit chiral response through their dis-

symmetric juxtaposition, the angle between those segments diminishes. In the limit of a very long, highly compressed helix, every local electric dipole lies almost in one plane, diminishing 3D point-pair chirality.

Beyond electric dipoles, a more detailed analysis of the chiroptical properties of these nanohelices would need to take into account electric quadrupoles. In plasmonic nanoparticles, such quadrupoles can arise from retardation effects,^[63] from the gradient of the electric field of light within the material or from the shape of the nanostructures.^[64] For chiral plasmonic nanoparticles, electric quadrupoles can play an important role in the nonlinear chiroptical interactions, as has been demonstrated in the case of second harmonic generation.^[25]

Although third harmonic Rayleigh scattering shares similarities with second harmonic Rayleigh scattering (e.g., the intensity of the signal follows a power law dependence on the intensity of incident light), there are several important differences. At the fundamental level, within the electric dipole approximation, whereas the detected second harmonic emission typically originates from the surface of the nanostructures, THRS originates from the entire volume of the nanostructures. From an experimental point of view, in the case of THRS, the larger separation between the frequency of illumination and that of the third harmonic offers practical advantages. On the

one hand side, illumination in the visible part of the spectrum allows to access harmonic frequencies in the UV, where many chiral molecules have a strong response. On the other hand side, it is possible to access the strong chiroptical resonances of plasmonic nanoparticles by illuminating them at near-IR, where the nanoparticles are much less susceptible to optical damage.

Finally, we need to consider the effect of nanohelix sedimentation during measurements. Traditional chiroptical effects in the linear optical regime (such as, circular dichroism or optical rotatory dispersion) depend very strongly on the optical path length and the concentration. We have previously demonstrated that due to non-negligible weight of the nanohelices, there is a small gradient of concentration in our measurement cuvettes (see Figure 5a in ref. [38]). To complement these data, here, we investigated the variations of CD spectra in the linear regime as a function of time. The results are shown in Figure S6, Supporting Information. They show that over a period of 3 h, there is a very small effect on the CD, which is negligible on the time scale of our data acquisition for THRS (30 s). Moreover, compared to CD in the linear regime, the dependence of THRS on the concentration of nanohelices is much less dramatic. The reason is that whereas the linear chiroptical techniques are measured against the overwhelming background of transmitted light that does not interact with chiral scatterers, in the case of THRS, the signal originates only from interactions with the chiral scatterers. Increasing their concentration increases the intensity of the third harmonic light but not the chiroptical contrast. As a consequence, THRS is applicable to tiny volumes of illumination, where the traditional, linear regime chiroptical techniques are not practical. However, high particle concentration can still have a significant effect on the THRS results, via multiple scattering events and associated linear/Rayleigh chiroptical scattering.

4. Conclusion

In conclusion, we have presented the first report of THRS OA. This new nonlinear chiroptical effect has been observed from silver nanohelices, randomly dispersed and freely revolving in a 3D isotropic liquid environment. Upon varying the illumination wavelength, the effect always clearly occurs at the third-harmonic and is recorded well above the multiphoton background. The measured third-harmonic signal follows a cubic power dependence and no evidence of laser-induced sample damage is observed during our experiments.

We also present the first theoretical treatment of the effect in a helical geometry. Our simple continuum discrete-dipole model of the nanohelix readily indicates a physically sensible upper bound on the possible extent of chiral discrimination in third-harmonic scattering, approached by samples in the present study. It also indicates that to secure greater discrimination, the most successful strategy may be fabricating nanohelices of greater length, that is, more twists, rather than changing the pitch angle, and that it may be worth investigating coils of narrower cross-section.

Together with the recently reported second harmonic hyper Rayleigh scattering effect,[38] THRS OA forms the basis of an entirely new type of “hyper (Rayleigh) chiroptical spectroscopy” capable of probing increasing orders of chiral hyperpolarizabilities in organic and inorganic chiral structures. Fourth harmonic Rayleigh scattering optical activity can readily be envisioned as

a logical next step. This novel spectroscopy can provide a lot more information, compared to linear optics, because of the numerous tensor elements in the nonlinear hyperpolarizabilities’ tensors. Although these tensor elements have long been regarded as a complexity barrier, recent progress suggests that it is possible to tackle the problem using machine learning approaches.[65] Such an analysis could offer an unprecedented understanding of chiral optical interactions, for instance by revealing the role of electric and magnetic dipolar and multipolar contributions.

5. Experimental Section

Sample Preparation: The nano GLancing Angle Deposition (nanoGLAD) technique is employed to grow tridimensional chiral nanohelices, as reported previously.[15]

Initially, a hexagonal array of Au dots (10 nm diameter), with 90 nm spacing between them, was prepared on a silicon wafer (2-inch) by means of block-copolymer micelle nanolithography.[66] To summarize this method, the block-copolymer micelles of poly(styrene)-*b*-poly(2-vinylpyridine) (PVP units: 495; PS units: 1056) containing Au salts in the core were formed by self-assembly in toluene. Subsequently, they were spin-coated onto the Si wafer, where the micelles form a quasihexagonally ordered monolayer (with spacing ≈ 90 nm). Plasma treatment reduced the Au salts to form metallic nanodots with ≈ 10 nm in diameter. These Au dots acted as seeds for the following GLAD treatment.

The Ag–Ti nanohelices were then grown from the Au dots array using a GLAD system that allowed co-deposition from dual electron-beam evaporators (base pressure of 1×10^{-6} mbar). The substrate was cooled down to 90 K with liquid nitrogen for 1 h and positioned at an angle of 87° with respect to the direction of flux. The alloy stoichiometry was controlled by the deposition rates for each evaporator that was independently measured by a quartz crystal microbalance (QCM). The nanohelices were grown with 700 nm thickness of Ag including $\approx 3\%$ Ti through the whole body of the nanohelices (based on the QCMs) while rotating the substrate for 720° (i.e., full rotation twice) with $1.8 \pm 0.1^\circ/\text{nm}$ of the azimuthal rotation rate per unit thickness.[67] The direction of rotation (clockwise or anticlockwise) determined the handedness of the nanohelices.

As a final step, the grown Ag–Ti nanohelices were lifted off from the wafer by sonicating a piece of sample wafer ($\approx 1 \text{ cm}^2$) in an aqueous solution of 1 mM trisodium citrate for ≈ 5 min to prepare a stock solution. To minimize the effect of possible variations in structure and concentration, the same wafer with nanohelices was used for all experiments.

Dynamic Light Scattering: Colloidal solutions (≈ 0.5 mL) of both chiral nanohelices were measured over $5\times$ using a zeta potential analyzer (Zetasizer Nano ZS, Malvern). The material property of nanohelices was fixed to Ag (RI: 0.135, absorption: 3.990) and the environmental parameter was water (RI: 1.333, absorption: 0).

Linear Regime Chiroptical Characterization: Circular dichroism and extinction experiments were performed on an applied photophysics Chirascan circular dichroism spectrophotometer equipped with a Peltier temperature controller using the 10 mm path length of a 10×4 mm quartz cuvette. The ellipticity in Figure 1e is obtained from the formula

$$\theta \text{ (deg.)} = \frac{180}{\pi} \arctan \left(\frac{\sqrt{I_{\text{RCP}}} - \sqrt{I_{\text{LCP}}}}{\sqrt{I_{\text{RCP}}} + \sqrt{I_{\text{LCP}}}} \right) \approx \frac{180}{\pi} \Delta A(\lambda) \left(\frac{\ln 10}{4} \right) \quad (5)$$

where I_{RCP} and I_{LCP} denote the intensity of RCP and LCP light, respectively, and

$$\Delta A(\lambda) = A_{\text{LCP}} - A_{\text{RCP}} \quad (6)$$

is the difference in the attenuation of LCP and RCP light transmitted through the cuvette at a wavelength λ . The background corresponding to 1 mM trisodium citrate and cuvette’s absorption was subtracted from

subsequent measurements. The measurements in the 300–800 nm region were recorded using a standard photomultiplier tube (PMT) accessory, with the following measurement parameters: step 1 nm, time-per-point 0.5 s, monochromator bandwidth 10 nm. The measurements in the 400–1130 nm region were recorded using an IR3 Extended NIR PMT with the following measurement parameters: step 1 nm, time-per-point 0.5 s, monochromator bandwidth 10 nm. All measurements were made at 20 °C.

Third-Harmonic (Hyper) Rayleigh Scattering Experiments: A Spectra Physics Mai Tai Ti:sapphire laser pumped a Radiantis Inspire optical parametric oscillator (OPO). The idler beam produced by the OPO (≈ 200 fs pulse width, 80 MHz repetition rate) was modulated by an optical chopper (50% duty cycle) and passed through an achromatic half-wave plate (used for laser power control), an uncoated calcite Glan-Laser polarizer with transmission axis aligned vertically, and an achromatic quarter-wave plate to obtain CPL. A couple of longpass filters removed light with wavelength below 950 nm. An achromatic lens (focal length = 30 mm) focused the laser beam into a fused quartz cuvette containing nanoparticle suspension. A lens (focal length = 25 mm) collected and collimated light scattered at the right angle to the incident beam. Another lens (focal length = 200 mm) focused the collected light onto a photocathode of a PMT. A hard-coated bandpass filter in front of the PMT transmitted light in the selected wavelength range (full-width at half-maximum = 10 nm). For the power dependence experiments, a filter centered at the third of the incident wavelength was used. To obtain emission spectra, measured for 20 mW incident power, measurements were done with various filters in front of the PMT.

Finite-Difference Time-Domain Simulations: A photonic simulation software (Lumerical) was employed to model the time dependent electromagnetic field properties of a left-handed nanohelix. The dimensions of the helix were as shown in Figure 1b.

The nanohelices were silver. Hence, a Johnson and Christy material model was used to compute the refractive index of silver (as a function of λ) in the finite-difference time-domain (FDTD) simulations. The spatial extent of the Eulerian meshed simulation region was $1 \mu\text{m} \times 1 \mu\text{m} \times 1.5 \mu\text{m}$; the boundaries of the domain were perfectly matched layers. The void was a perfect vacuum and the initial temperature of the helix was 300 K. The distance between nodes in the mesh was globally 8.5 nm; the region surrounding the nanohelix was locally refined to a node spacing of 1 nm to improve resolution and accuracy.

Left- and right-handed CPL was incident on the nanohelix from a distance of approximately a half-wavelength. The response of the nanohelix was computed for two different incident wavelengths of light at which the corresponding mode strength of the electric and magnetic field was extracted. The first simulation set was at the fundamental wavelength (1095 nm; FWHM 500 nm; pulse duration 5.6 fs) and the second set was at the third-harmonic wavelength (365 nm; FWHM 250 nm; pulse duration 1.6 fs).

The FDTD simulation processed 1 ps of light propagation. The orientation of the nanohelix was permuted such that the effect of the direction from which the pulse of light came could be determined. For both left- and right-handed CPL, the direction of propagation was tested along all three of the Cartesian axes.

Supporting Information

Supporting Information is available from the Wiley Online Library or from the author.

Acknowledgements

V.K.V. acknowledges support from the Royal Society through the University Research Fellowships and the Royal Society grants PEF1\170015, ICA\R1\201088, and RGF\EA\180228, as well as, the STFC grant ST/R005842/1. L.O. and V.K.V. acknowledge funding and support from the Engineering and Physical Sciences Research Council (EPSRC) Centre for Doctoral Training in Condensed Matter Physics (CDT-CMP), Grant No.

EP/L015544/1. V.K.V. further acknowledges EPSRC grant EP/T001046/1. D.M.R. and G.D.P. acknowledge support from the EPSRC through grant EPSRC DTP EB- BB 1250.

Conflict of Interest

The authors declare no conflict of interest.

Data Availability Statement

The data that support the findings of this study are openly available in the repository of the University of Bath at <https://doi.org/10.15125/BATH-01064>.^[68]

Keywords

chirality, metamaterials, nanophotonics, nonlinear optics, plasmonics

Received: April 29, 2021

Revised: July 27, 2021

Published online:

- [1] D. Androić, D. S. Armstrong, A. Asaturyan, T. Averett, J. Balewski, K. Bartlett, J. Beaufait, R. S. Berniniwaththa, J. Benesch, F. Benmokhtar, J. Birchall, R. D. Carlini, J. C. Cornejo, S. C. Dusa, M. M. Dalton, C. A. Davis, W. Deconinck, J. Diefenbach, J. F. Dowd, J. A. Dunne, D. Dutta, W. S. Duvall, M. Elaasar, W. R. Falk, J. M. Finn, T. Forest, C. Gal, D. Gaskell, M. T. W. Gericke, J. Grames, et al., *Nature* **2018**, 557, 207.
- [2] H. Jiao, L. Wachsmuth, S. Kumari, R. Schwarzer, J. Lin, R. O. Eren, A. Fisher, R. Lane, G. R. Young, G. Kassiotis, W. J. Kaiser, M. Pasparakis, *Nature* **2020**, 580, 391.
- [3] A. Davison, P. Thomas, *Biol. Lett.* **2020**, 16, 20200110.
- [4] A. Adriani, A. Mura, G. Orton, C. Hansen, F. Altieri, M. L. Moriconi, J. Rogers, G. Eichstädt, T. Momary, A. P. Ingersoll, G. Filacchione, G. Sindoni, F. Tabataba-Vakili, B. M. Dinelli, F. Fabiano, S. J. Bolton, J. E. P. Connerney, S. K. Atreya, J. I. Lunine, F. Tosi, A. Migliorini, D. Grassi, G. Piccioni, R. Noschese, A. Cicchetti, C. Plainaki, A. Olivieri, M. E. O'Neill, D. Turrini, S. Stefani, et al., *Nature* **2018**, 555, 216.
- [5] H.-R. Yu, P. Motloch, U.-L. Pen, Y. Yu, H. Wang, H. Mo, X. Yang, Y. Jing, *Phys. Rev. Lett.* **2020**, 124, 101302.
- [6] M. E. Franks, G. R. Macpherson, W. D. Figg, *Lancet* **2004**, 363, 1802.
- [7] F. Kamarei, P. Vajda, F. Gritti, G. Guiochon, *J. Chromatogr. A* **2014**, 1345, 200.
- [8] D. J. Cordato, L. E. Mather, G. K. Herkes, *J. Clin. Neurosci.* **2003**, 10, 649.
- [9] B. S. Sekhon, *J. Mod. Med. Chem.* **2013**, 1, 10.
- [10] J. Mun, M. Kim, Y. Yang, T. Badloe, J. Ni, Y. Chen, C.-W. Qiu, J. Rho, *Light: Sci. Appl.* **2020**, 9, 139.
- [11] V. K. Valev, J. J. Baumberg, C. Sibilila, T. Verbiest, *Adv. Mater.* **2013**, 25, 2517.
- [12] J. T. Collins, C. Kuppe, D. C. Hooper, C. Sibilila, M. Centini, V. K. Valev, *Adv. Opt. Mater.* **2017**, 5, 1700182.
- [13] J. B. Pendry, *Science* **2004**, 306, 1353.
- [14] D. Schamel, M. Pfeifer, J. G. Gibbs, B. Miksch, A. G. Mark, P. Fischer, *J. Am. Chem. Soc.* **2013**, 135, 12353.
- [15] A. G. Mark, J. G. Gibbs, T.-C. Lee, P. Fischer, *Nat. Mater.* **2013**, 12, 802.
- [16] M. Khorasaninejad, W. T. Chen, A. Y. Zhu, J. Oh, R. C. Devlin, D. Rousso, F. Capasso, *Nano Lett.* **2016**, 16, 4595.

- [17] E. Hendry, T. Carpy, J. Johnston, M. Popland, R. V. Mikhaylovskiy, A. J. Laphorn, S. M. Kelly, L. D. Barron, N. Gadegaard, M. Kadodwala, *Nat. Nanotechnol.* **2010**, *5*, 783.
- [18] R. Farshchi, M. Ramsteiner, J. Herfort, A. Tahraoui, H. T. Grahn, *Appl. Phys. Lett.* **2011**, *98*, 162508.
- [19] J. F. Sherson, H. Krauter, R. K. Olsson, B. Julsgaard, K. Hammerer, I. Cirac, E. S. Polzik, *Nature* **2006**, *443*, 557.
- [20] H.-E. Lee, H.-Y. Ahn, J. Mun, Y. Y. Lee, M. Kim, N. H. Cho, K. Chang, W. S. Kim, J. Rho, K. T. Nam, *Nature* **2018**, *556*, 360.
- [21] K. Oxenoid, Y. Dong, C. Cao, T. Cui, Y. Sancak, A. L. Markhard, Z. Grabarek, L. Kong, Z. Liu, B. Ouyang, Y. Cong, V. K. Mootha, J. J. Chou, *Nature* **2016**, *533*, 269.
- [22] M. J. Urban, C. Zhou, X. Duan, N. Liu, *Nano Lett.* **2015**, *15*, 8392.
- [23] X. Lan, Z. Chen, G. Dai, X. Lu, W. Ni, Q. Wang, *J. Am. Chem. Soc.* **2013**, *135*, 11441.
- [24] A. Qu, M. Sun, J.-Y. Kim, L. Xu, C. Hao, W. Ma, X. Wu, X. Liu, H. Kuang, N. A. Kotov, C. Xu, *Nat. Biomed. Eng.* **2021**, *5*, 103.
- [25] V. K. Valev, J. J. Baumberg, B. De Clercq, N. Braz, X. Zheng, E. J. Osley, S. Vandendriessche, M. Hojeij, C. Blejean, J. Mertens, C. G. Biris, V. Volskiy, M. Ameloot, Y. Ekinci, G. A. E. Vandenbosch, P. A. Warburton, V. V. Moshchalkov, N. C. Panouli, T. Verbiest, *Adv. Mater.* **2014**, *26*, 4074.
- [26] S. Chen, F. Zeuner, M. Weismann, B. Reineke, G. Li, V. K. Valev, K. W. Cheah, N. C. Panouli, T. Zentgraf, S. Zhang, *Adv. Mater.* **2016**, *28*, 2992.
- [27] L. D. Barron, *Chem. Phys. Lett.* **1986**, *123*, 423.
- [28] D. C. Hooper, A. G. Mark, C. Kuppe, J. T. Collins, P. Fischer, V. K. Valev, *Adv. Mater.* **2017**, *29*, 1605110.
- [29] J. T. Collins, D. C. Hooper, A. G. Mark, C. Kuppe, V. K. Valev, *ACS Nano* **2018**, *12*, 5445.
- [30] B. Ritchie, *Phys. Rev. A* **1975**, *12*, 567.
- [31] B. Ritchie, *Phys. Rev. A* **1976**, *13*, 1411.
- [32] B. Ritchie, *Phys. Rev. A* **1976**, *14*, 359.
- [33] B. Ritchie, *Phys. Rev. A* **1976**, *14*, 1396.
- [34] T. Verbiest, M. Kauranen, Y. V. Rompaey, A. Persoons, *Phys. Rev. Lett.* **1996**, *77*, 1456.
- [35] E. Plum, X.-X. Liu, V. A. Fedotov, Y. Chen, D. P. Tsai, N. I. Zheludev, *Phys. Rev. Lett.* **2009**, *102*, 113902.
- [36] A. Belardini, M. C. Larciprete, M. Centini, E. Fazio, C. Sibilila, D. Chiappe, C. Martella, A. Toma, M. Giordano, F. B. de Mongeot, *Phys. Rev. Lett.* **2011**, *107*, 257401.
- [37] D. L. Andrews, T. Thirunamachandran, *J. Chem. Phys.* **1979**, *70*, 1027.
- [38] J. T. Collins, K. R. Rusimova, D. C. Hooper, H.-H. Jeong, L. Ohnoutek, F. Pradaux-Caggiano, T. Verbiest, D. R. Carbery, P. Fischer, V. K. Valev, *Phys. Rev. X* **2019**, *9*, 011024.
- [39] D. Verreault, K. Moreno, É. Merlet, F. Adamietz, B. Kauffmann, Y. Ferland, C. Olivier, V. Rodriguez, *J. Am. Chem. Soc.* **2020**, *142*, 257.
- [40] L. Ohnoutek, N. H. Cho, A. W. A. Murphy, H. Kim, D. M. Rășădean, G. D. Pantoș, K. T. Nam, V. K. Valev, *Nano Lett.* **2020**, *20*, 5792.
- [41] P. W. Atkins, L. D. Barron, *Proc. R. Soc. London, Ser. A* **1968**, *304*, 303.
- [42] G. Wagnière, *J. Chem. Phys.* **1982**, *77*, 2786.
- [43] F. Hache, H. Mesnil, M. C. Schanne-Klein, *Phys. Rev. B* **1999**, *60*, 6405.
- [44] H. Mesnil, F. Hache, *Phys. Rev. Lett.* **2000**, *85*, 4257.
- [45] R. Cameron, G. C. Tabisz, *Mol. Phys.* **1997**, *90*, 159.
- [46] S. A. Akhmanov, V. I. Zharikov, *J. Exp. Theor. Phys. Lett.* **1967**, *6*, 137.
- [47] G. S. He, M. J. Cho, W. J. Kim, A. Baev, A. Urbas, P. N. Prasad, *Adv. Opt. Mater.* **2013**, *1*, 763.
- [48] S. P. Rodrigues, S. Lan, L. Kang, Y. Cui, P. W. Panuski, S. Wang, A. M. Urbas, W. Cai, *Nat. Commun.* **2017**, *8*, 14602.
- [49] I. Tinoco, *J. Chem. Phys.* **1975**, *62*, 1006.
- [50] L. De Boni, C. Toro, F. E. Hernández, *Opt. Lett.* **2008**, *33*, 2958.
- [51] C. Toro, L. De Boni, N. Lin, F. Santoro, A. Rizzo, F. E. Hernandez, *Chem. - Eur. J.* **2010**, *16*, 3504.
- [52] H. J. Singh, Saumitra, V. R. Singh, S. K. Sikdar, B. Jayaprakash, A. Ghosh, *ACS Photonics* **2016**, *3*, 863.
- [53] W. Kuhn, *Trans. Faraday Soc.* **1930**, *26*, 293.
- [54] D. P. Shelton, *J. Chem. Phys.* **2018**, *149*, 224504.
- [55] J. S. Ford, D. L. Andrews, *J. Phys. Chem. A* **2018**, *122*, 563.
- [56] D. L. Andrews, *Symmetry* **2020**, *12*, 1466.
- [57] D. L. Andrews, G. A. Jones, A. Salam, R. G. Woolley, *J. Chem. Phys.* **2018**, *148*, 040901.
- [58] D. L. Andrews, *J. Opt.* **2018**, *20*, 033003.
- [59] T. M. Lowry, *Optical Rotatory Power*, Longmans, Green and Co., Ltd., London **1935**; republished by Dover Publications, Inc., New York **1964**.
- [60] A. Passaseo, M. Esposito, M. Cuscunà, V. Tasco, *Adv. Opt. Mater.* **2017**, *5*, 1601079.
- [61] C. Bustamante, I. Tinoco, M. F. Maestre, *J. Chem. Phys.* **1982**, *76*, 3440.
- [62] G. H. Wagnière, G. L. J. A. Rikken, *Chem. Phys. Lett.* **2009**, *481*, 166.
- [63] I. Russier-Antoine, E. Benichou, G. Bachelier, C. Jonin, P. F. Brevet, *J. Phys. Chem. C* **2007**, *111*, 9044.
- [64] J. Mun, J. Rho, *Opt. Lett.* **2018**, *43*, 2856.
- [65] R. Wang, F. Liang, Z. Lin, *Sci. Rep.* **2020**, *10*, 3486.
- [66] R. Glass, M. Möller, J. P. Spatz, *Nanotechnology* **2003**, *14*, 1153.
- [67] H.-H. Jeong, A. G. Mark, M. Alarcón-Correa, I. Kim, P. Oswald, T.-C. Lee, P. Fischer, *Nat. Commun.* **2016**, *7*, 11331.
- [68] L. Ohnoutek, R. Jones, B. Olohan, D. Rasadean, D. Pantos, V. Valev, University of Bath Research Data Archive, Bath **2021**, <https://doi.org/10.15125/BATH-01064>.